

Article

# Catalytic Behaviour of Flame-Made CuO-CeO<sub>2</sub> Nanocatalysts in Efficient CO Oxidation

Feng Zhao <sup>1,2</sup>, Shuangde Li <sup>1</sup>, Xiaofeng Wu <sup>1</sup>, Renliang Yue <sup>1</sup>, Weiman Li <sup>1,2</sup>, Xicuo Zha <sup>1,2</sup>, Yuzhou Deng <sup>1,2</sup> and Yunfa Chen <sup>1,3,\*</sup>

<sup>1</sup> State Key Laboratory of Multi-Phase Complex Systems, Institute of Process Engineering, Chinese Academy of Sciences, Beijing 100190, China; zhaofeng@ipe.ac.cn (F.Z.); sdli@ipe.ac.cn (S.L.); wxftsjc@ipe.ac.cn (X.W.); rlyue@ipe.ac.cn (R.Y.); wml@ipe.ac.cn (W.L.); zhaxicuo@ipe.ac.cn (X.Z.); yzdeng@ipe.ac.cn (Y.D.)

<sup>2</sup> University of Chinese Academy of Sciences, Beijing 100049, China

<sup>3</sup> Center for Excellence in Regional Atmospheric Environment, Institute of Urban Environment, Chinese Academy of Sciences, Xiamen 361021, China

\* Correspondence: chenyf@ipe.ac.cn; Tel.: +86-10-8254-4896

Received: 5 February 2019; Accepted: 8 March 2019; Published: 13 March 2019



**Abstract:** CuO-CeO<sub>2</sub> nanocatalysts with varying CuO contents (1, 5, 9, 14 and 17 wt %) were prepared by one-step flame spray pyrolysis (FSP) and applied to CO oxidation. The influences of CuO content on the as-prepared catalysts were systematically characterized by X-ray diffraction (XRD), N<sub>2</sub> adsorption-desorption at −196 °C, field emission scanning electron microscopy (FESEM), high-resolution transmission electron microscopy (HRTEM), Raman spectroscopy, X-ray photoelectron spectroscopy (XPS), and hydrogen-temperature programmed reduction (H<sub>2</sub>-TPR). A superior CO oxidation activity was observed for the 14 wt % CuO-CeO<sub>2</sub> catalyst, with 90% CO conversion at 98 °C at space velocity (60,000 mL × g<sup>−1</sup> × h<sup>−1</sup>), which was attributed to abundant surface defects (lattice distortion, Ce<sup>3+</sup>, and oxygen vacancies) and high reducibility supported by strong synergistic interaction. In addition, the catalyst also displayed excellent stability and resistance to water vapor. Significantly, in situ diffuse reflectance infrared Fourier transform spectroscopy (in situ DRIFTS) showed that in the CO catalytic oxidation process, the strong synergistic interaction led readily to dehydroxylation and CO adsorption on Cu<sup>+</sup> at low temperature. Furthermore, in the feed of water vapor, although there was an adverse effect on the access of CO adsorption, there was also a positive effect on the formation of fewer carbon intermediates. All these results showed the potential of highly active and water vapor-resistive CuO-CeO<sub>2</sub> catalysts prepared by FSP.

**Keywords:** flame spray pyrolysis; synergistic interaction; CO oxidation; CuO-CeO<sub>2</sub> nanocatalyst; water resistance; carbon intermediate

## 1. Introduction

Owing to increasingly stringent environmental regulations, the development of materials with high activity as three-way catalysts (TWCs) for removing CO becomes necessary. The traditional supported noble metal catalysts (e.g., Pt, Pd and Rh) offer excellent catalytic properties with the low CO oxidation temperature. However, it is limited for their application due to the cost, easy sintering and coking [1]. In recent years, research has focused on the metal oxides for their economy and readily controlling activities [2,3]. In particular, the combination of copper oxides (CuO<sub>x</sub>) and CeO<sub>2</sub> is of great interest as a result of their cooperative redox and catalytic activities [4,5]. The activity of CuO<sub>x</sub>/CeO<sub>2</sub> catalysts is related to the highly dispersed CuO<sub>x</sub> species, its strong interaction with CeO<sub>2</sub>, and mutual effect between Cu<sup>1+/2+</sup> and Ce<sup>3+/4+</sup> redox couples [6]. The CO oxidation reaction mechanism follows a Mars van Krevelen, starting with CO adsorption on Cu<sup>+</sup>, and then reacts with

lattice oxygen to produce the carbon intermediates, such as mono- or poly-dentate carbonates and bidentate carbonate. Finally, desorption of intermediates produces CO<sub>2</sub> [7]. The CO oxidation rate over CuO/CeO<sub>2</sub> catalysts correlates with the formation of the Cu<sup>+</sup>-CO above a crucial temperature as Cu<sup>+</sup>-CO formation is the rate-limiting step [8]. However, the CO catalytic oxidation reaction is also affected by carbon intermediates, which is related to CO<sub>2</sub> desorption below the threshold temperature, hindering further adsorption of fresh CO molecule and retarding the reaction rate [9,10]. Additionally, the catalytic activity of CuO-CeO<sub>2</sub> is usually negatively affected by water vapor, which limits their practical application. For example, Bae et al. [11] reported that with 14% H<sub>2</sub>O in the feed, the reaction temperature increased by around 60 and 40 °C respectively for the 10 and 20 at % Cu-CeO<sub>2</sub> catalysts prepared by co-precipitation method in the CO catalytic oxidation. Thus, it is highly desired to develop highly efficient and stabilized CO catalytic materials, especially with a strong water resistive property.

It is well known that the dispersion and valence state of copper species, solid solution, and oxygen vacancies associated with the synergistic interaction and catalytic performance strongly depend on the preparation methods. For example, Wang et al. [12] reported that the solvent-free method facilitated the formation of synergistic interaction between copper species and ceria to result in smaller crystallite size and the formation of more Cu<sup>+</sup> species together with a high ratio of Ce<sup>3+</sup>. Shang et al. [13] founded that the impregnation method offered more highly dispersed CuO and stronger synergistic interaction between CuO and CeO<sub>2</sub> to promote the reduction of CuO to Cu<sup>+</sup> species at the Cu-Ce interface, resulting in the highest catalytic activity, whereas the catalyst prepared by the co-precipitation method suppressed the formation of the Cu-Ce interface, where the adsorbed CO would react with active lattice oxygen to form CO<sub>2</sub> to exhibit a lower catalytic performance. Besides, the water resistive property of CuO-CeO<sub>2</sub> catalytic systems is also affected by preparation methods [14]. Flame spray pyrolysis (FSP) is a comparatively simple, one-step synthesis for mixed metal oxides [15]. Metal precursors experience a high-temperature and oxygen-rich environment in the flame, and also the rapid quench leads to strong synergistic interaction between the highly dispersed active component and support, as well as formation of more oxygen defects [16]. Moreover, most research has paid attention on the physicochemical-activity relationships of CuO-CeO<sub>2</sub> catalysts in CO oxidation, and few works in the literature has reported the relationships among physicochemical properties, the evolution of intermediates (such as hydroxyl groups, CO adsorbed center Cu<sup>n+</sup> and carbon intermediates) and catalytic activity.

Considering this fact, in order to prepare the CuO-CeO<sub>2</sub> catalyst with low temperature CO oxidation activity and high water resistance, as well as reveal the catalytic behaviour, in this work, a range of catalysts with 1–17 wt % CuO were prepared via FSP, and the physical, chemical, morphological and surface electronic properties of the catalysts were systematically characterized by X-ray diffraction (XRD), N<sub>2</sub> adsorption-desorption at −196 °C, field emission scanning electron microscopy (FESEM), high-resolution transmission electron microscopy (HRTEM), Raman, X-ray photoelectron spectroscopy (XPS) and hydrogen-temperature programmed reduction (H<sub>2</sub>-TPR). Moreover, much attention has been paid to the intermediates of CO catalytic oxidation with and without water vapor via in situ diffuse reflectance infrared Fourier transform spectroscopy (in situ DRIFTS).

## 2. Materials and Methods

### 2.1. Catalysts' Preparation

The FSP method was used for synthesis of CuO-CeO<sub>2</sub> mixed oxide catalysts with different nominal CuO to CeO<sub>2</sub> mass concentration of 1, 5, 9, 14 and 17 wt %. The details of the FSP device and the section view of the spray nozzle were depicted in the report [16]. The precursor solution was prepared by dissolving Cu(CH<sub>3</sub>COO)<sub>2</sub> (Aladdin, Shanghai, China, >98%) and Ce(CH<sub>3</sub>COO)<sub>3</sub>·H<sub>2</sub>O (Mackin, Shanghai, China, 99.9%) into 200 mL propionic acid (Sinopharm, Shanghai, China, 99.9%) to obtain 0.2 M Ce precursor solutions. During the process of preparation, the precursor solution was

fed (rate: 5 mL/min) to the flame by a syringe pump and atomized with dispersion oxygen (rate: 3 L/min), and then the dispersed droplets of precursor were ignited by a surrounding supporting flame (1.5 L/min CH<sub>4</sub>, 3 L/min O<sub>2</sub>). The gas flow rate was monitored by mass flow controller (D07-11C, Beijing Sevenstar Electronics Co., Ltd., Beijing, China). The productive powder was gathered with glass fiber filters with the aid of a vacuum pump and scraped from the filter for direct use as a catalyst. Pure CeO<sub>2</sub> and bulk CuO samples were also produced as a comparison with 0.2 M metal concentration precursors. The catalysts with different CuO loadings (1, 5, 9, 14 and 17 wt %) were denoted as 1, 5, 9, 14 and 17% CuCe, respectively.

## 2.2. Catalysts' Characterization

XRD patterns were collected on PANalytical B.V. Empyrean powder diffractometer (Almelo, Netherlands) at a scan speed of 0.0248°/s in the range of 10–90° with Cu K $\alpha$  radiation (40 kV, 40 mA).

The specific surface area, the pore volume and pore size of the samples were determined from the adsorption and desorption isotherms of nitrogen at –196 °C using an SSA-7300 (Beijing Builder Electronic Technology Co., Beijing, China) apparatus, the catalysts (ca. 100 mg) were out gassed at 150 °C under vacuum for 5 h before measurement.

The morphologies of the catalysts were collected at  $\times 60,000$  magnification by FESEM (JOEL, JSM 7001F, Akishima, Japan) with energy-dispersive X-ray spectroscopy (EDX) signal detection. HRTEM images were acquired by a JEM 2100F electron microscopy (JEOL, 200KV). The sample was prepared by dipping a copper-grid supported transparent carbon foil in an ethanol solution, and the grid was dried in the open air.

The Raman spectra were conducted from 200 to 800 cm<sup>–1</sup> on a Renishaw RM2000 (Wotton-under-Edge, UK) using a laser wavelength of 532 nm with a power of 1.25 mW on the sample (objective 50 $\times$ ), the accumulations of spectra were 10 scans.

H<sub>2</sub>-TPR measurement was performed on AutoChemisorbII 2920 pulse chemisorption system equipped with a TCD detector (Micromeritics, Norcross, GA, USA) and a TPx (temperature-programmed controller and software) system. 50 mg of the sample was reduced under 25 mL/min of 10% H<sub>2</sub>/N<sub>2</sub> along with temperature rising up to 700 °C at a 10 °C/min ramping rate.

X-ray powder surface species of the as-prepared catalysts were determined by XPS using an XLESCALAB 250Xi electron spectrometer from VG Scientific (Thermo Fisher Scientific, Waltham, MA, USA), using a monochromatic Al K $\alpha$  radiation. The binding energies were calibrated with respect to the C 1s energy of incidental graphitic carbon at 284.8 eV. The surface compositions of all samples in terms of atomic ratios were calculated, using a Shirley-type background and empirical cross section factors for XPS transmission.

In situ DRIFTS were collected by using a Fourier transform infrared spectrometer (Vertex 70, Bruker, Billerica, MA, USA), equipped with a reaction cell (PIKE, Fitchburg, WI, USA) and an MCT detector. The spectra were averaged over 32 scans with a resolution of 4 cm<sup>–1</sup>. Prior to measurement, the catalyst was pretreated at 300 °C in a N<sub>2</sub> flow (70 mL/min<sup>–1</sup>) for 30 min to remove contaminants from the catalyst surface. After cooling down to 25 °C, the background spectrum was collected. Then a stream (70 mL/min<sup>–1</sup>) of 1 vol % CO, 0.6 vol % O<sub>2</sub>, balanced with N<sub>2</sub> (the same atmosphere as the CO catalytic oxidation test) was introduced to the reaction cell.

## 2.3. Catalytic Activity Measurement

The catalytic activity was carried out using a conventional fixed-bed quartz reactor (10 mm inner diameter). The catalyst (70 mg, 40–60 mesh) mixed with quartz sand (140 mg) with quartz wool packed at both ends of the catalyst bed was loaded in the quartz reactor. The gas mixture of 1 vol % CO, 0.6 vol % O<sub>2</sub> and balance with N<sub>2</sub> was passed through the reactor for CO catalytic oxidation. The total flow rate was 70 ml  $\times$  min<sup>–1</sup>, matching a weight hourly space velocity (WHSV) at 60,000 mL  $\times$  g<sup>–1</sup>  $\times$  h<sup>–1</sup>. The test was stabilized at each temperature for 60 min, the outlet products were measured with on-line gas chromatography (Shimadzu GC-2014, Kyoto, Japan) equipped with a

flame ionization detector (FID), and another FID with a conversion furnace for converting CO<sub>2</sub> to CH<sub>4</sub> was used to analyse the concentration of CO<sub>2</sub> in the outlet gas. A K-type thermocouple was placed in the middle of the catalyst bed to measure the temperature of the catalyst.

The complete conversion values of CO ( $\eta_{CO}$ ) and the yield of CO<sub>2</sub> ( $\eta_{CO_2}$ ) were calculated according to the following equations:

$$\eta_{CO} = \frac{C_{CO,in} - C_{CO,out}}{C_{CO,in}} \times 100\% \quad (1)$$

$$\eta_{CO_2} = \frac{C_{CO_2,out}}{C_{CO,in}} \times 100\% \quad (2)$$

$C_{CO,in}$  (ppm),  $C_{CO,out}$  (ppm) and  $C_{CO_2,out}$  (ppm) were the concentrations of CO in the inlet and outlet gas, and CO<sub>2</sub> in the outlet gas, respectively.

### 3. Results and Discussion

#### 3.1. Microstructure of the Prepared Catalysts

The X-ray patterns of the catalysts are compiled in Figure 1. All patterns exhibit the featured peaks of the cubic fluorite structure of CeO<sub>2</sub> (JCPDS 034-0394), and also two small diffraction peaks of CuO (JCPDS 044-0706) are detected at 35.5 and 38.9° with CuO from 9 wt %, which indicates copper species are aggregating on the CeO<sub>2</sub> support, for CuO displays very limited solubility in CeO<sub>2</sub> framework. The particle sizes of the catalysts are calculated by the Scherrer equation, and the results are listed in Table 1. With the introduction of copper species, the crystallite sizes of the samples become larger stemming from the presence of foreign dopants during the high-temperature particle formation in the FSP process leading to the thermal sintering effect [17]. Interestingly, the crystallite size of the 14% CuCe sample shrinks, together with the smallest cell parameter, which stem from the smaller ionic radius of Cu<sup>2+</sup> ions (0.073 nm) than either Ce<sup>4+</sup> (0.097 nm) or Ce<sup>3+</sup> ions (1.14 nm), as shown in Table 1. The result shows that the largest amounts of Cu<sup>2+</sup> ions are located into the CeO<sub>2</sub> framework to form a Cu-Ce-O solid solution [18], favoring the redox reaction of CO catalytic oxidation.

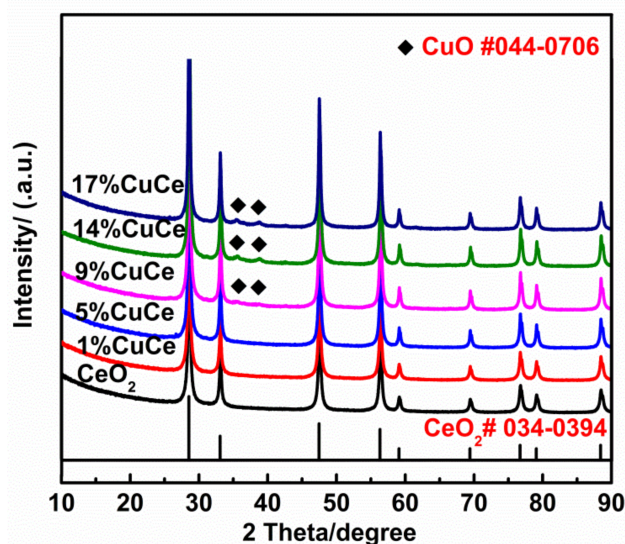


Figure 1. X-ray diffraction (XRD) patterns of the prepared samples.

Figure A1 presents the N<sub>2</sub> adsorption-desorption isotherms and the pore size distributions of the obtained samples. The pore belongs to the type IV isotherm with a H3 hysteresis loop ( $p/p_0 > 0.4$ ), as shown in Figure A1a, meaning the pore structure is mesoporous, which is further verified by the pore size distribution (Figure A1b). The pore volumes and pore sizes of these samples are in the range of 0.15 to 0.20 cm<sup>3</sup> × g<sup>-1</sup> and 9.10 to 13.60 nm, respectively. With the increment of CuO contents,

the surface areas of the catalysts linearly decrease from  $54.2$  to  $38.9 \text{ m}^2 \times \text{g}^{-1}$  (Table 1), which is attributed to aggregation of the large particles of CuO [19], and in agreement with the XRD results. It is notable that the sequence of the surface areas of the CuO-CeO<sub>2</sub> catalysts is not in accordance with the catalytic activity discussed in the following section, revealing that the specific surface area is not the primary factor to affect the catalytic activity for CO oxidation.

**Table 1.** Physical properties of various catalysts.

Samples	Crystallite Size <sup>a</sup> (nm)	Cell Parameter (nm)	Surface Area ( $\text{m}^2 \times \text{g}^{-1}$ )	Pore Volume ( $\text{cm}^3 \times \text{g}^{-1}$ )	Pore Size (nm)
CeO <sub>2</sub>	25.6	0.5421	54.2	0.18	9.46
1% CuCe	26.5	0.5420	48.5	0.16	9.10
5% CuCe	30.1	0.5420	43.9	0.17	10.30
9% CuCe	31.6	0.5419	42.6	0.20	13.60
14% CuCe	31.4	0.5417	39.4	0.15	11.50
17% CuCe	32.8	0.5422	38.9	0.16	10.46

<sup>a</sup> Calculated applying the Scherrer formula.

The 14% CuCe sample was subjected to field emission scanning electron microscopy with energy dispersive X-ray spectroscopy (FESEM-EDX) analysis to obtain information about element dispersion, as shown in Figure A2. Cu, Ce and O elements exhibit the homogeneous distributions with related peaks of various elements distinctly observed in the spectra and their proportions. The simultaneous nucleation of Cu and Ce in the flame along with the rapid-quenching stage can enhance the formation of atomic-scale dispersed active element sites [20], which is feasible for the interaction between CuO and CeO<sub>2</sub> during the reaction.

The morphological transformation of the samples with the incorporation of the copper was investigated and the results are depicted in Figure A3. The particles sizes estimated from HRTEM images are approximately from 15–40 nm, which is compliant with the crystallite sizes calculated by the Scherrer formula. The pure CeO<sub>2</sub> displays rhombohedral morphology (Figure A3a). Upon doping with 1 wt % CuO, the morphology of the catalyst is not obviously changed (Figure A3b). As the CuO contents are further increased, the morphology of samples transform to polyhedral (the 5 and 9% CuCe samples, Figure A3c,d), through to sphere (the 14 and 17% CuCe samples, Figure A3e,f), suggesting the preferential growth directions of the crystals are disrupted by the introduction of copper [21].

HRTEM measurement also provides the microstructures of the samples. For CuO-CeO<sub>2</sub> catalysts, the lattice fringes of 0.29–0.32 nm presenting on Figure 2a–d can be indexed to the (111) crystal planes of CeO<sub>2</sub>. It is worthy of note that the 14% CuCe sample exhibits the smallest lattice spacing of 0.29 nm, which is in agreement with the formation the most solid solutions observed in XRD, suggesting the existence of strongest synergistic interaction between the active components and the support [22]. Importantly, the lattice fringes of the 14% CuCe sample displays lattice distortions (which include bending and dislocation), as depicted in Figure 2e, which are induced by the copper ions dopants lowering the energy for oxygen vacancies segregation and mobility of lattice oxygen [23].

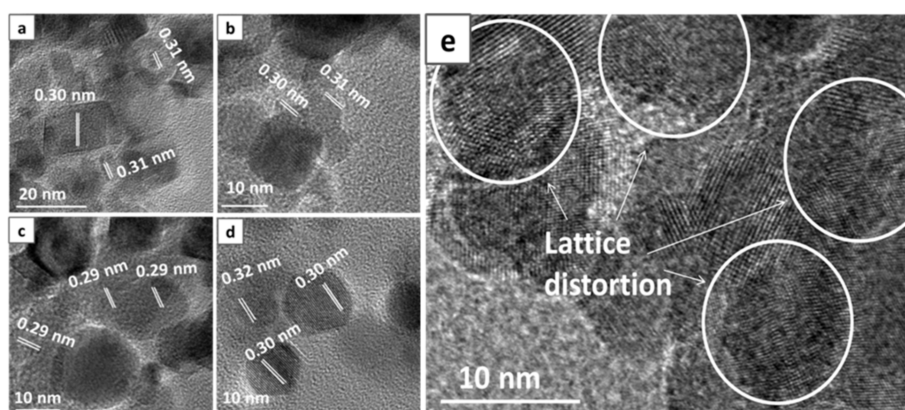


**Figure 2.** High resolution transmission electron microscopy (HRTEM) images of the representative samples: (a) 1% CuCe; (b) 9% CuCe; (c) 14% CuCe; (d) 17% CuCe; (e) high magnification of the 14% CuCe sample.

Raman spectra (Figure 3) were used to further investigate the structure of the catalysts. The observed main band of pure  $\text{CeO}_2$  is  $463\text{ cm}^{-1}$ , which is ascribed to the triple degenerate  $F_{2g}$  mode of ceria [24]. With increasing CuO contents, except the 1% CuCe sample, the slight red shifts of the  $F_{2g}$  Raman bands of the Cu-containing samples suggest the incorporation of Cu atoms into the  $\text{CeO}_2$  lattice [25]. The oxygen vacancies caused by the crystalline distortion are also investigated by Raman spectra. The band  $O_V$  at  $606\text{ cm}^{-1}$  can be attributed to Frenkel-type anion defects [26]. The relative intensity ratio between the defect band ( $I_{O_V}$ ) and the  $F_{2g}$  band ( $I_{F_{2g}}$ ) of the fluorite phase can be used as an indicator of the oxygen vacancies [27]. Figure 4b displays the trend of the  $O_V/F_{2g}$  values. It is obvious the oxygen vacancy changes with increasing of CuO content in a volcano-shaped tendency. The 14% CuCe sample displays the most amounts of oxygen vacancies.

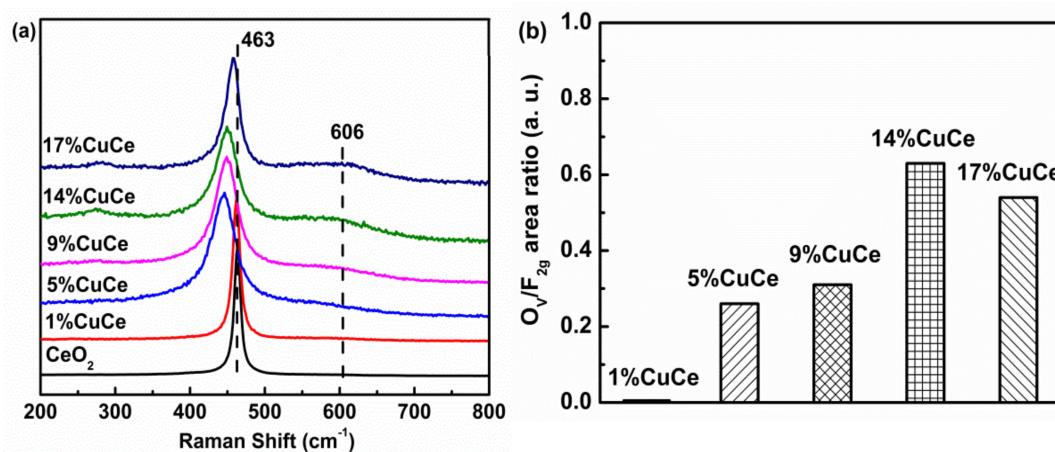


**Figure 3.** (a) Raman spectra for the prepared samples; (b)  $O_V/F_{2g}$  area ratios of the Cu-containing catalysts.

### 3.2. The Surface Composition of Catalysts

In order to obtain information on the surface element distribution, we analyzed the Cu 2p, Ce 3d and O 1s (Figure 4) by XPS measurement. The ratio values of Cu to Ce are listed in Table 2. Comparing with the nominal values of Cu/Ce of the samples, the values obtained by XPS are 3–16 times higher, which further confirms the high dispersion of Cu species detected by FESEM results. Figure 4a displays two groups of peaks for the Cu-containing catalysts: the peak at 928.9–939.8 eV is assigned to Cu  $2p_{3/2}$ , while the peak at 950.2–958.7 eV belongs to Cu  $2p_{1/2}$  [28]. Both peaks are further de-convoluted into  $\text{Cu}^{2+}$  (935.1–939.8 eV and 954.8–958.7 eV for  $2p_{3/2}$  and  $2p_{1/2}$ , separately) and  $\text{Cu}^+$

or  $\text{Cu}^0$  (928.9–935.1 eV and 950.2–954.8 eV for  $2p_{3/2}$  and  $2p_{1/2}$ , separately). The relevant satellites exist in the 940.1–944.0 eV ( $\text{Cu}^+$  or  $\text{Cu}^0$   $2p_{3/2}$ ), 945.5–947.3 eV ( $\text{Cu}^+$  or  $\text{Cu}^0$   $2p_{1/2}$ ) and 960.9–968.0 eV ( $\text{Cu}^{2+}$   $2p_{1/2}$ ) ranges [29]. In order to discern between  $\text{Cu}^0$  and  $\text{Cu}^+$  as a very tiny difference in peak position, the Auger  $L_3VV$  lines are further investigated. The peaks in the Auger kinetic spectra 915.4 and 917.5 eV correspond to  $\text{Cu}^+$  and  $\text{Cu}^{2+}$  species, respectively (Figure A4). By contrast, the peak of  $\text{Cu}^0$  in Cu  $L_3VV$  spectrum is generally at 918.7 eV, but the current peaks arise in lower kinetic energy, which suggests no existence of  $\text{Cu}^0$ , meanwhile confirming the presence of  $\text{Cu}^+$ . The values of  $\text{Cu}^{2+}/\text{Cu}$  are calculated by de-convoluted spectra, and listed in Table 2. The copper species on the 1% CuCe sample is fully  $\text{Cu}^+$  ions. A small number of copper species can easily form  $\text{Cu}^+$ , because of the similarity of  $\text{Cu}^+$  and  $\text{Ce}^{4+}$  ionic radii [30]. With the increment of CuO contents, the ratios of  $\text{Cu}^{2+}$  are monotonically increased from 0 to 67.2% (Table 2), as  $\text{Ce}^{4+}$  ions are continuously substituted by copper ions, there are more  $\text{Cu}^{2+}$  formed to maintain the electronic neutrality of the lattice [31]. This trend is further confirmed by the high kinetic energy shift of the broad peaks (from 915.4 to 917.1 eV) in the spectra of Cu  $L_3VV$  Auger (Figure A4).

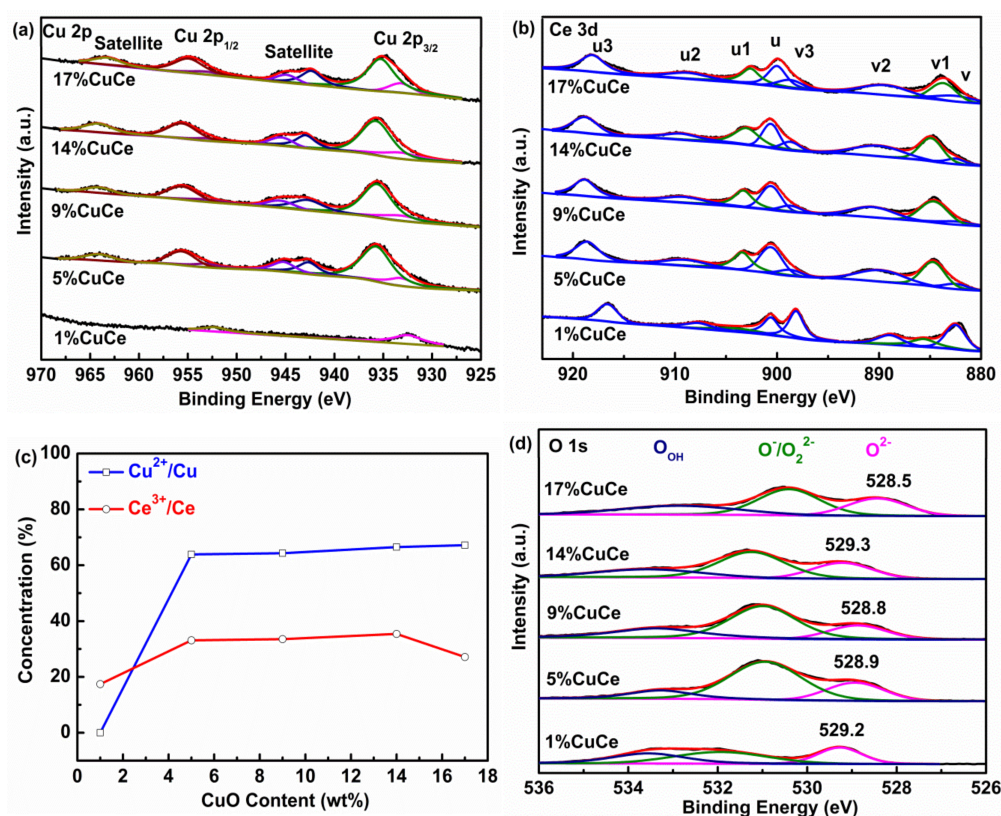


**Figure 4.** (a) Cu 2p X-ray photoelectron spectroscopy (XPS) spectra; (b) Ce 3d XPS spectra; (c) the variation tendency of ratios of  $\text{Cu}^{2+}$  and  $\text{Ce}^{3+}$  for the samples with different CuO contents; (d) O 1s XPS spectra.

**Table 2.** Catalytic performance and surface chemical properties of various catalysts.

Samples	T <sub>50</sub> (°C)	T <sub>90</sub> (°C)	E <sub>a</sub> (kJ × mol <sup>-1</sup> )	Cu/Ce (at. %)		Cu <sup>2+</sup> /Cu (%)	Ce <sup>3+</sup> /Ce (%)
				Nominal	XPS		
CeO <sub>2</sub>	176	233	63.2	-	-	-	-
1% CuCe	114	149	124.4	0.02	0.32	0	17.4
5% CuCe	110	123	99.4	0.11	0.56	63.9	33.1
9% CuCe	88	104	40.8	0.19	0.69	64.3	33.5
14% CuCe	74	98	28.9	0.30	1.04	66.5	35.4
17% CuCe	129	139	87.0	0.37	1.08	67.2	27.1
Bulk CuO	174	195	121.8	-	-	-	-

The coexistence of Cu<sup>+</sup> and Cu<sup>2+</sup> is linked to the redox cycle of Ce<sup>3+</sup> ↔ Ce<sup>4+</sup> [32]. Ce 3d spectra can be de-convoluted into three pairs of spin-orbit doublets shown in Figure 4b. The characteristic peaks denoted as v (at 882.5 eV), v2 (at 889.6 eV) and v3 (at 898.7 eV) belong to Ce<sup>4+</sup> 3d<sub>5/2</sub>, and the characteristic peaks marked as u (at 900.6 eV), u2 (at 907.7 eV) and u3 (at 916.6 eV) are features of Ce<sup>4+</sup> 3d<sub>3/2</sub>, the other two peaks denoted as v1 (at 885.6 eV) and u1 (at 903.9 eV) are ascribed to Ce<sup>3+</sup> 3d<sub>5/2</sub> and Ce<sup>3+</sup> 3d<sub>3/2</sub>, separately [33]. The relative contents of Ce<sup>3+</sup>/Ce over the surfaces of the catalysts are calculated from the sum of areas of Ce<sup>3+</sup> to the entire cerium and listed in Table 2. The Ce<sup>3+</sup>/Ce values vary as a volcano-shaped curve with increasing CuO content (Figure 4c). The 14% CuCe sample possesses the highest values of Ce<sup>3+</sup>/Ce (35.4%) than other catalysts, which is in good agreement with the largest amounts of oxygen vacancies verified by Raman.

The trends of the ratios of Cu<sup>2+</sup>/Cu and Ce<sup>3+</sup>/Ce of the samples are depicted in Figure 4c. As CuO contents increasing from 1 to 14 wt %, both the ratios of Cu<sup>2+</sup> and Ce<sup>3+</sup> in the CuO-CeO<sub>2</sub> catalysts increase concurrently. These results provide evidence of the existence of redox equilibrium of Cu<sup>2+</sup> + Ce<sup>3+</sup> ↔ Cu<sup>+</sup> + Ce<sup>4+</sup>, which has been claimed to be the origin of a synergistic interaction in the CuO-CeO<sub>2</sub> catalysts [34]. During the flame synthesis process, the redox equilibrium progressively shifts to the left to simultaneously increase the ratios of Cu<sup>2+</sup> and Ce<sup>3+</sup> as more copper species incorporation, suggesting electrons transfer from copper oxide clusters to ceria support, and the electronic synergistic interaction achieves the maximum on the 14% CuCe sample. Nevertheless, as the CuO content is further increased to 17 wt %, the ratio of Ce<sup>3+</sup> of the sample declines with the opposite variation trend compared with the ratio of Cu<sup>2+</sup>, meaning the synergistic interaction turns to weakening.

The O 1s spectra can be de-convoluted into three contributions, as shown in Figure 4c. The peaks at 528.9–529.7 eV, 530.6 and 531.5–532.7 eV, which are ascribed to the lattice oxygen (O<sup>2-</sup>), surface adsorbed oxygen (O<sup>-</sup>/O<sub>2</sub><sup>2-</sup>) and hydroxyl oxygen (O<sub>OH</sub>), respectively [35]. The O<sup>2-</sup> peak position of the 14% CuCe sample displays higher binding energy value (529.3 eV) than those of other samples (528.5–529.2 eV) originating from “O → Cu” and “O → Ce” electron transfer, which promotes the instability of lattice oxygen, and improves the mobility of lattice oxygen [22]. Moreover, the results further confirm that the CeO<sub>2</sub> lattice is distorted by the introduction of Cu ions as observed in the HRTEM results, because the lattice distortion lowers the energy for lattice oxygen release [36]. In the CO catalytic oxidation reaction, the gaseous O<sub>2</sub> is trapped by oxygen vacancies, and transfers to the active surface lattice oxygen; after the reactions of adsorbed CO with surface lattice oxygen, the subsurface lattice oxygen readily refilled the oxygen surface [37].

### 3.3. Redox Properties of the Prepared Catalysts

The H<sub>2</sub>-TPR experiment is plotted on Figure 5. Pristine CeO<sub>2</sub> displays a broad peak centred at 275 °C, which is ascribed to the surface reduction of CeO<sub>2</sub> [38]. The 1 and 5% CuCe samples exhibit two reduction peaks (labelled α and β), which are attributed to the reduction of highly dispersed CuO<sub>x</sub> species and Cu<sup>+</sup>/Cu<sup>2+</sup> ions into the ceria lattice, respectively [29,39]. Besides α and β peaks, another reduction peak γ belongs to the bulk CuO appears on the samples with the increment of CuO contents from 9 wt % [40], which is in accordance with the XRD results. With the introduction of Cu, the tendency of the low-temperature reduction peak indicates that the coexistence of CuO

and CeO<sub>2</sub> promotes the surface reducibility, and the 14% CuCe sample exhibits the lowest reduction temperature. The 14% CuCe sample can weaken the strength of the Ce-O bond through the strong synergistic interaction between CuO<sub>x</sub> and CeO<sub>2</sub> species and promote desorption of the surface lattice oxygen from the CeO<sub>2</sub> surface, thereby enhancing the redox property of the catalyst [7].

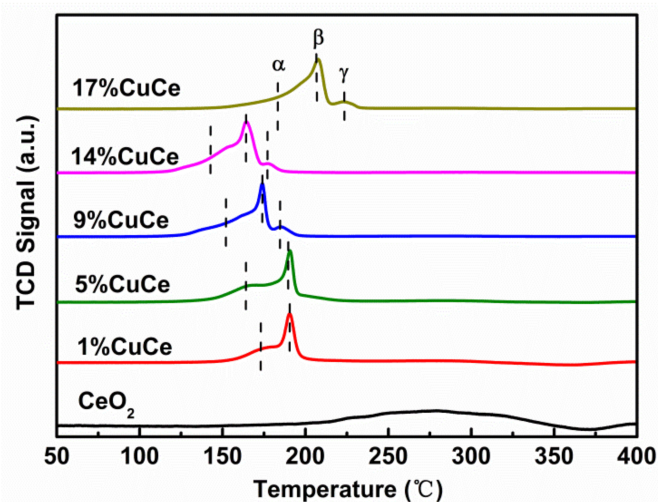


Figure 5. Hydrogen-temperature programmed reduction (H<sub>2</sub>-TPR) profile of the prepared samples.

### 3.4. The CO Catalytic Oxidation Performance

Figure 6a shows the CO conversion as a function of reaction temperature at WHSV = 60,000 mL × g<sup>-1</sup> × h<sup>-1</sup> over the prepared samples. The temperatures of 50 and 90% CO conversion (T<sub>50</sub> and T<sub>90</sub>) are summarized in Table 2. The pure CeO<sub>2</sub> has very limited activity for CO oxidation with T<sub>50</sub> = 176 °C, T<sub>90</sub> = 233 °C, and the bulk CuO exhibits low CO catalytic activity with T<sub>50</sub> = 174 °C, T<sub>90</sub> = 195 °C. After incorporation of CuO, the CO oxidation performances of the CuO-CeO<sub>2</sub> samples are obviously improved, which is attributed to a synergistic interaction between CuO and CeO<sub>2</sub>. With the increment of CuO, the catalytic performances of the CuO-CeO<sub>2</sub> samples also display as a volcano-shape tendency, and the 14% CuCe sample exhibits the optimal catalytic activity, achieving T<sub>50</sub> = 74 °C, T<sub>90</sub> = 98 °C.

The kinetic study is conducted for all these catalysts based on the CO conversion not exceeding 10%, following first-order kinetics [41]:

$$\gamma_{CO} = \frac{N_{CO} \times \eta_{CO}}{m_{CO}} \quad (3)$$

$$\gamma_{CO} = -\kappa c = \left[ -A \exp\left(-\frac{E_a}{RT}\right) \right] c \quad (4)$$

where  $N_{CO}$  is the CO gas flow rate (mL/min),  $\eta_{CO}$  is the CO conversion,  $m_{CO}$  is the catalyst weight (g), and  $\gamma$ ,  $\kappa$ ,  $A$ , and  $E_a$  are the reaction rate (mmol × g<sup>-1</sup> × s<sup>-1</sup>), pre-exponential factor, rate constant (s<sup>-1</sup>), and apparent activation energy (kJ × mol<sup>-1</sup>), respectively.

The reaction rate for CO oxidation at T = 80 °C for all samples are shown in Figure 6b. The reaction rate of the 14% CuCe sample is 1.82 mmol × g<sup>-1</sup> × h<sup>-1</sup>, which is obviously larger than these of other samples (0–0.62 mmol × g<sup>-1</sup> × h<sup>-1</sup>). The Arrhenius plots for the CO oxidation are displayed in Figure 6c. The activation energies  $E_a$  are on account of the slopes of the Arrhenius plots between ln( $\gamma \times 10^{-5}$ ) versus 1000/T and listed in Table 2. The results show that the  $E_a$  values decreased in the following sequence: 14% CuCe < 9% CuCe < CeO<sub>2</sub> < 17% CuCe < 5% CuCe < Bulk CuO < 1% CuCe, which confirms the superior catalytic performance of the 14% CuCe sample. Moreover, compared with CuO-CeO<sub>2</sub> catalysts prepared by other methods from the literature (Table 3), a nearly full CO conversion at a temperature of 120 °C in the present work was better than the previous 1MnOx-5CuO

(Mn/Cu molar of 1:5)-FSP, 0.4% mol CuO-SCS, 10 wt % CuO-IMP, 14.1 mol % CuO-ST, 5 wt % CuO-MN, 1 wt % Pd-IMP, and 4 Co<sub>3</sub>O<sub>4</sub> (Co/Ce = 4/1)-STA.

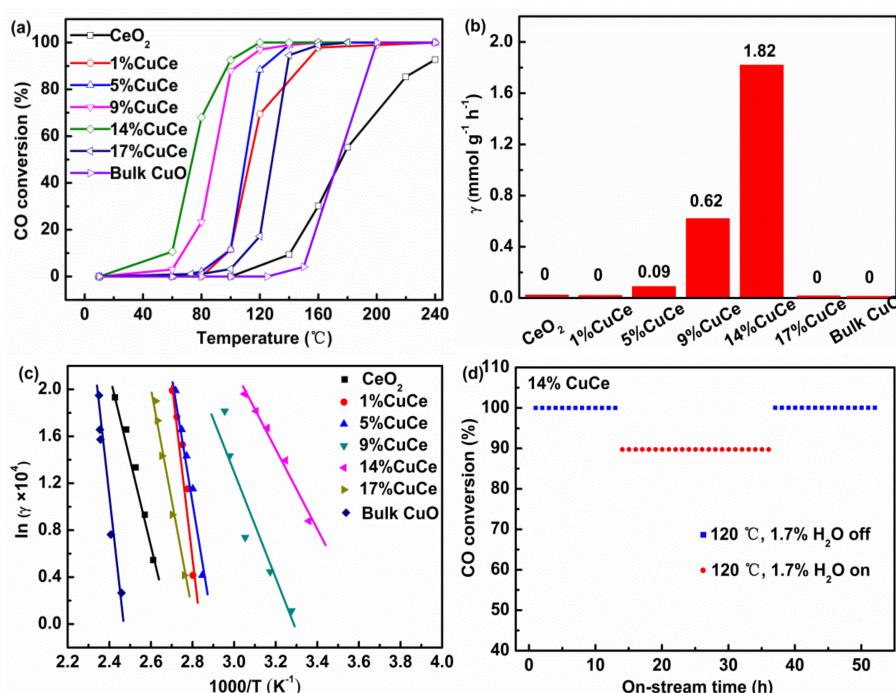


**Figure 6.** (a) the curve of CO conversion; (b) the reaction rate of all catalysts at 80 °C; (c) Arrhenius plots of catalytic CO oxidation over all samples; (d) the effect of water vapor on the activities of the 14% CuCe sample at 120 °C. (weight hourly space velocity (WHSV): 60,000 mL × g<sup>-1</sup> × h<sup>-1</sup>; 1 vol % CO, 0.6 vol % O<sub>2</sub>).

**Table 3.** Comparison on CO oxidation activity over CeO<sub>2</sub> based catalysts via different methods.

Sample	Preparation	CO Conversion (%)	Reaction Condition	Ref.
14 wt % CuO-CeO <sub>2</sub>	FSP	100 (120 °C)	1% CO/0.6% O <sub>2</sub> /N <sub>2</sub> , 60,000 mL × g <sup>-1</sup> × h <sup>-1</sup>	This work
1MnO <sub>x</sub> -5CuO-CeO <sub>2</sub>	FSP	100 (160 °C)	1% CO/0.6% O <sub>2</sub> /N <sub>2</sub> , 60,000 mL × g <sup>-1</sup> × h <sup>-1</sup>	[17]
Cu <sub>0.40</sub> Ce <sub>0.60</sub>	SCS <sup>a</sup>	100 (130 °C)	1000 ppm CO/10%O <sub>2</sub> /N <sub>2</sub> , 30,000 mL × g <sup>-1</sup> × h <sup>-1</sup>	[42]
10 wt % CuO-CeO <sub>2</sub>	IMP <sup>b</sup>	99 (117 °C)	4% CO/10% O <sub>2</sub> /N <sub>2</sub> , 9000 mL × g <sup>-1</sup> × h <sup>-1</sup>	[43]
14.1 mol % CuO-CeO <sub>2</sub> NR	ST <sup>c</sup>	100 (150 °C)	1% CO/10% O <sub>2</sub> /N <sub>2</sub> , 60,000 mL × g <sup>-1</sup> × h <sup>-1</sup>	[44]
5 wt % CuO-CeO <sub>2</sub>	MN <sup>d</sup>	100 (200 °C)	1% CO/Air, 30,000 mL × g <sup>-1</sup> × h <sup>-1</sup>	[45]
1 wt % Pd/CeO <sub>2</sub> -rod	IMP	100 (150 °C)	2% CO/2% O <sub>2</sub> /He, 60,000 mL × g <sup>-1</sup> × h <sup>-1</sup>	[46]
4Co <sub>3</sub> O <sub>4</sub> -CeO <sub>2-x</sub>	STA <sup>e</sup>	100 (160 °C)	1% CO/1.6% O <sub>2</sub> /He, 30,000 mL × g <sup>-1</sup> × h <sup>-1</sup>	[47]

<sup>a</sup> Solution combustion synthesis; <sup>b</sup> Impregnation; <sup>c</sup> Solvent thermal; <sup>d</sup> Mechanochemical nanocasting; <sup>e</sup> Sequential templating approach.

To investigate the stability and effect of water vapor on the catalytic performances of the 14% CuCe sample, the on-stream reactions at 120 °C were implemented in the feed of water vapor (Figure 6d). The catalyst maintains full conversion at 120 °C over the first 13 h of running without water vapor. In the following 23 h CO stream with the feed of 1.7% H<sub>2</sub>O, it can be found that water vapor has little negative effect on the catalyst, resulting in the CO conversion from 100 to 89.8%. Interestingly, after removing water vapor, the catalytic activity is fast recovered. The results suggest that the 14% CuCe catalyst has long stability and high resistance to water vapor. During the flame synthesis process, high temperature of the flame (>1000 °C) is in favor of the formation of the metal oxide with enhanced stability [16]. Furthermore, the synergistic effect originating from electron transfer between active species and support often plays a pivotal role in water resistance of the catalysts [48].

### 3.5. CO and O<sub>2</sub> Co-Adsorption In Situ Diffuse Reflectance Infrared Fourier Transform Spectroscopy (DRIFTS) Analysis

In order to study the nature of intermediates of CO catalytic reaction, in situ DRIFTS analysis was examined. Figure 7 presents the DRIFTS spectra recorded under operando CO + O<sub>2</sub> reaction stream over CuO-CeO<sub>2</sub> catalysts with different copper contents at the temperature from 25 to 240 °C. The bands in the 3800–3000 cm<sup>-1</sup> range correspond to hydroxyl groups. Note that the area of the hydroxyl band shows negative values because hydroxyls are removed during the reactions. The initial temperature of dehydroxylation of the 14% CuCe sample is at 60 °C, which is significantly lower than those of other samples, suggesting the hydroxyl groups are readily removed for a good accessibility of the active center in the catalytic oxidation reaction [8]. Sanchez et al. reported the degree of difficulty of surface removal of OH<sup>-</sup> correlated with the reducibility of the catalyst [49]. The zone in 2400–1900 cm<sup>-1</sup> is predominantly composed of the vibrations of two species, CO<sub>2</sub> and Cu<sup>n+</sup>-CO species, as observed on Figure 7, including the generation of CO<sub>2</sub> represented by the rotational vibration at 2360 and 2341 cm<sup>-1</sup>, and the 2250–1950 cm<sup>-1</sup> range, where a single band at 2100 cm<sup>-1</sup> corresponding to the Cu<sup>+</sup>-CO carbonyl is observed [8,50], suggesting Cu<sup>+</sup> is providing CO adsorption sites. The areas of the Cu<sup>+</sup>-CO band of different catalysts monitored with the reaction temperature were fitted to curve and depicted in Figure A5. The maximum temperature of carbonyl coverage of the 14% CuCe sample (80 °C) is lower than those of other samples (100 °C), indicating that CO is readily adsorbed on the 14% CuCe sample at lower temperature. The synergistic interaction between CuO and CeO<sub>2</sub> support triggered by electron transfer of the 14% CuCe sample is beneficial for enhancing CO adsorption to promote the catalytic activity [51].

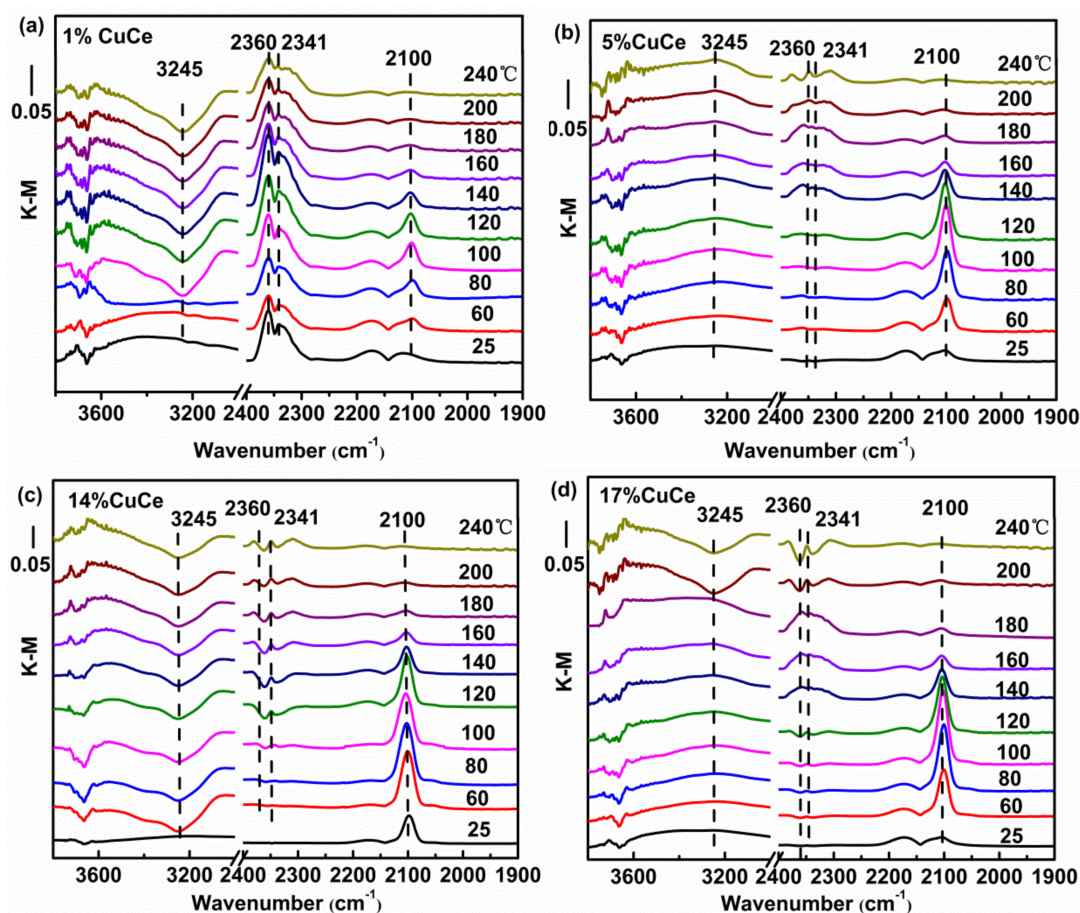


**Figure 7.** In situ DRIFTS spectra as a function of temperature from 25 to 240 °C under operando CO conditions with representative samples: (a) 1% CuCe; (b) 5% CuCe; (c) 14% CuCe; (d) 17% CuCe.

Figure 8 shows the variations of hydroxyl groups,  $\text{Cu}^+$ -CO and carbon intermediates without and with water vapor on the 14% CuCe sample. The bands below  $1700\text{ cm}^{-1}$  are attributed to the carbon intermediates (mainly bicarbonate and carbonates) [8]. With no presence of water vapor (Figure 8a),  $1570$  and  $1291\text{ cm}^{-1}$  bands are attributed to bicarbonate species [52], and the band at  $1465\text{ cm}^{-1}$  belongs to mono- or poly-dentate carbonates [53]. With 1.7%  $\text{H}_2\text{O}$  in the feed, the intensities of the  $\text{Cu}^+$ -CO bands of the sample become weakened, combining with accumulation of large amounts of hydroxyl groups on the surface, as shown in Figure 8b, which indicates a blocking effect induced by the presence of molecular water, limiting access of CO adsorption on  $\text{Cu}^+$ . Interestingly, the specific carbon species are modified after presence of water vapor. In the presence of water, the bands at  $1570\text{ cm}^{-1}$  keep the stability, while the bands at  $1465$  and  $1291\text{ cm}^{-1}$  become weak (Figure 8b,c), suggesting the formations of partial carbonates and bicarbonate decreased. Because the hydroxyl groups caused by water vapor on the catalyst surface play a key role in determining the nature of the carbon-based intermediates, which favor the formation of bicarbonates with respect to carbonates. Bicarbonates produce faster CO oxidation rates than carbonates [8]. Therefore, although there is an adverse effect for CO adsorption on  $\text{Cu}^+$ , fewer carbon intermediates, especially carbonates, generate on the interface of the catalysts with positive effect, which can still sustain the high CO conversion in the presence of water vapor. The spectra of the catalysts in the water vapor feed are invariable, as depicted in Figure 8d, which is consistent with the high stability of water resistance.

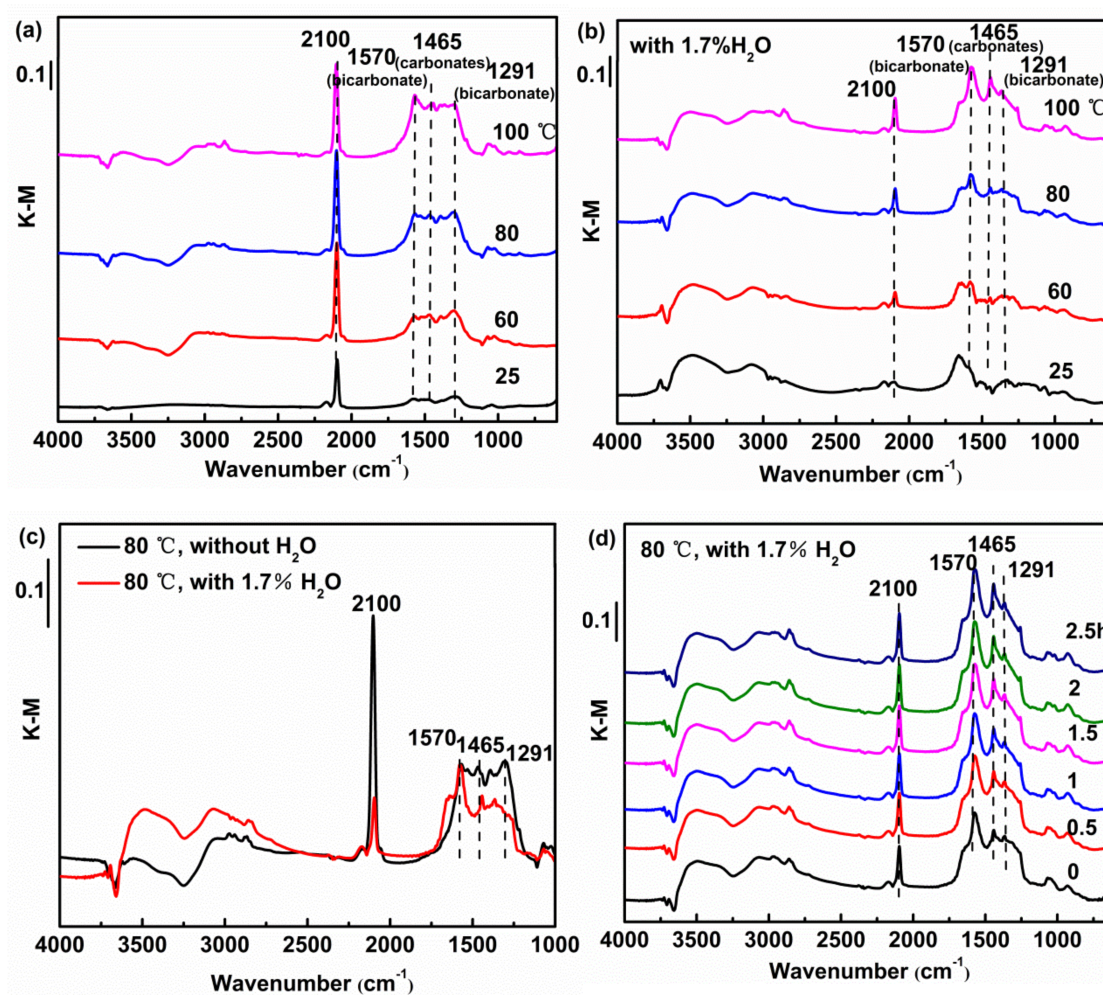


**Figure 8.** In situ DRIFT spectra of the 14% CuCe sample: (a) without water vapor from 25 to 120 °C; (b) with water vapor from 25 to 120 °C; (c) the comparison of CO catalytic oxidation with water vapor and without water vapor at 80 °C; (d) time evolution with water vapor at 80 °C.

#### 4. Conclusions

In this work, we investigated the effect of CuO contents on the physicochemical properties and CO catalytic behaviour of the flame-made CuO-CeO<sub>2</sub> catalyst. The 14% CuCe sample exhibited the best CO catalytic activity with T<sub>90</sub> at 98 °C, and good stability as well as high resistance to water vapor, which are ascribed to a greater number of defect sites (lattice distortions, Ce<sup>3+</sup> ions, and oxygen vacancies) and high reducibility originated from the strong synergistic interaction. The intermediate of CO catalytic oxidation reaction without and with water vapor were further investigated, the strong synergistic interaction leads readily to dehydroxylation and CO adsorption at low temperature. Importantly, with the presence of water vapor, although there is an adverse effect to the access of CO adsorption on Cu<sup>+</sup>, there is formation of less carbon intermediate, especially less carbonates, which exhibit a positive effect. These results demonstrate the FSP method is a rapid and effective strategy for preparing composite metal oxides nanocatalysts with a strong synergistic interaction among the oxides to improve the catalytic performance.

**Author Contributions:** Authors equally contributed to the conception, the design, the analysis of the experimental activity and to the writing of the paper.

**Funding:** This research described above was financially supported by the National Key Research and Development Program of China (2016YFC0204903, 2016YFC0207100, 2017YFC0702705 and 2017YFC0211503), the National Natural Science Foundation of China (No. 51672273), the National Hi-tech Research and Development Program of China (863 Program, 2012AA062702) and the Open Research Fund of State Key Laboratory of Multi-phase Complex Systems (No. MPCs-2017-D-06).

**Conflicts of Interest:** The authors declare no conflict of interest.

#### Appendix A

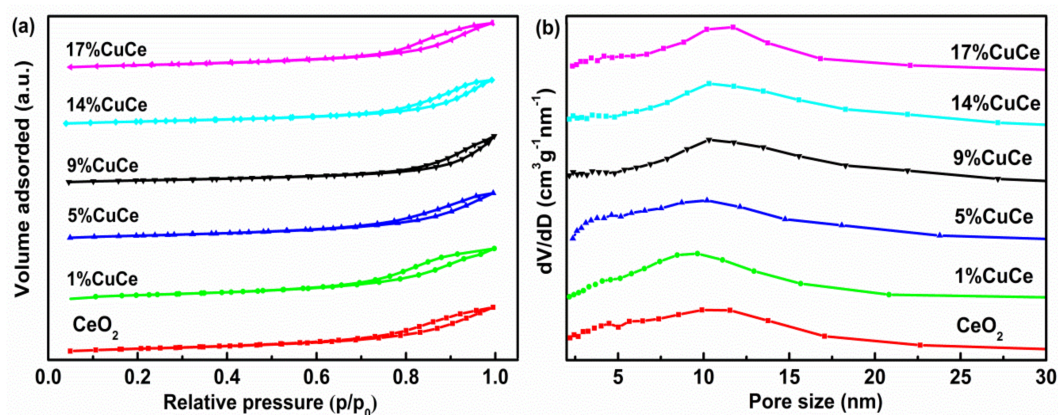


**Figure A1.** (a) N<sub>2</sub> adsorption-desorption isotherms curves; (b) pore size distribution calculated from the desorption branch of the prepared samples.

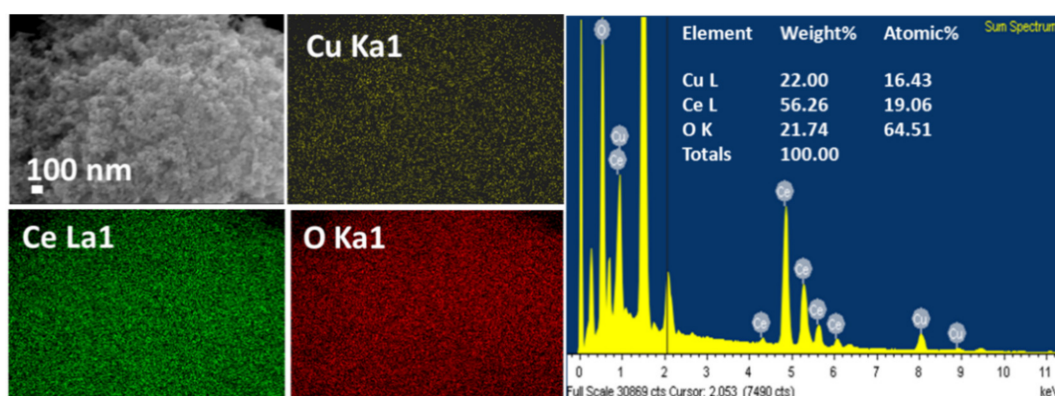


**Figure A2.** Field emission scanning electron microscopy (FESEM) images, element distributions and energy-dispersive X-ray spectroscopy (EDX) data for the 14% CuCe sample.

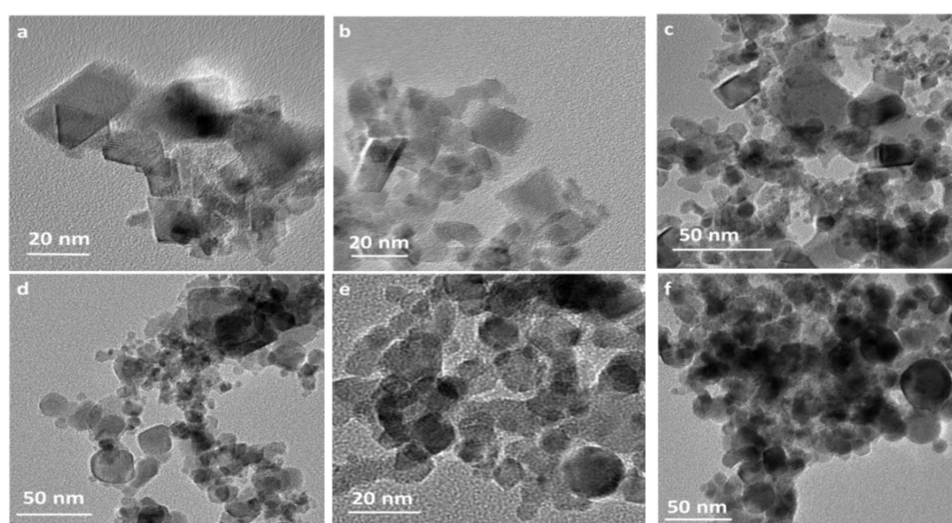


**Figure A3.** Morphologies of the prepared samples: (a) Pure CeO<sub>2</sub>; (b) 1% CuCe; (c) 5% CuCe; (d) 9% CuCe; (e) 14% CuCe; (f) 17% CuCe.

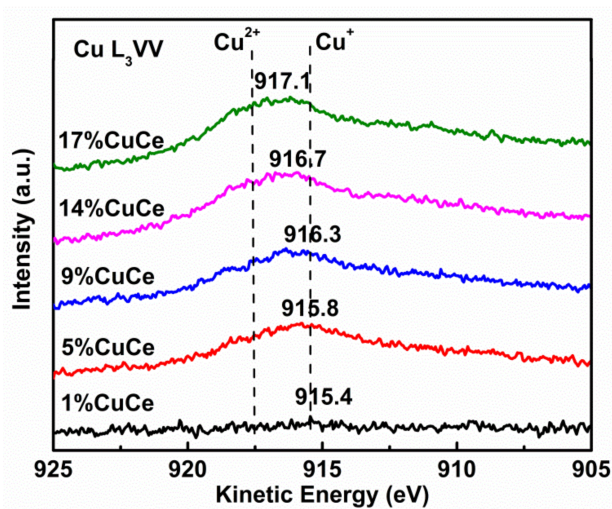


**Figure A4.** Kinetic energy spectra of Cu L<sub>3</sub>VV Auger.

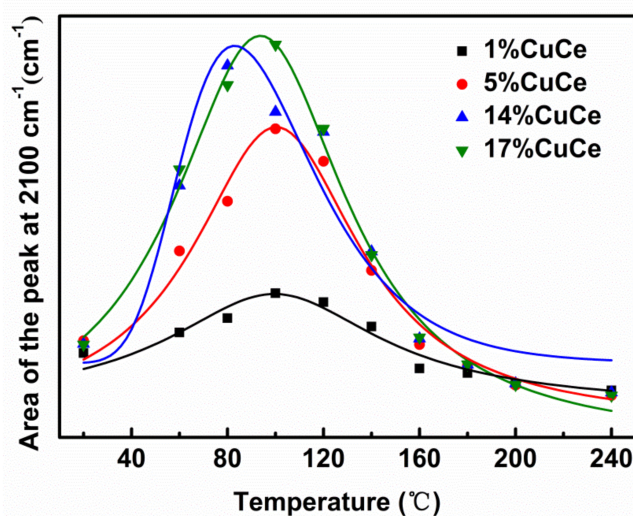


Figure A5. Integrated area of the  $\text{Cu}^+$ -CO band at  $2100\text{ cm}^{-1}$  as a function of temperature.

## References

- Pitkääho, S.; Matejova, L.; Jiratova, K.; Ojala, S.; Keiski, R.L. Oxidation of perchloroethylene-activity and selectivity of Pt, Pd, Rh, and  $\text{V}_2\text{O}_5$  catalysts supported on  $\text{Al}_2\text{O}_3$ ,  $\text{Al}_2\text{O}_3\text{-TiO}_2$  and  $\text{Al}_2\text{O}_3\text{-CeO}_2$ . Part 2. *Appl. Catal. B* **2012**, *126*, 215–224. [[CrossRef](#)]
- Varghese, S.; Cutrufello, M.G.; Rombi, E.; Cannas, C.; Monaci, R.; Ferino, I. CO oxidation and preferential oxidation of CO in the presence of hydrogen over SBA-15-templated  $\text{CuO-CeO}_2$  catalysts. *Appl. Catal. A* **2012**, *443–444*, 161–170. [[CrossRef](#)]
- Qiao, D.; Lu, G.; Liu, X.; Guo, Y.; Wang, Y.; Guo, Y. Preparation of  $\text{Ce}_{1-x}\text{Fe}_x\text{O}_2$  solid solution and its catalytic performance for oxidation of  $\text{CH}_4$  and CO. *J. Mater. Sci.* **2011**, *46*, 3500–3506. [[CrossRef](#)]
- Sedmak, G.; Hočevár, S.; Levec, J. Kinetics of selective CO oxidation in excess of  $\text{H}_2$  over the nanostructured  $\text{Cu}_{0.1}\text{Ce}_{0.9}\text{O}_{2-y}$  catalyst. *J. Catal.* **2003**, *213*, 135–150. [[CrossRef](#)]
- Avgouropoulos, G.; Ioannides, T.; Papadopoulou, C.; Batista, J.; Hocevar, S.; Matralis, H.K. A comparative study of Pt/ $\gamma\text{-Al}_2\text{O}_3$ , Au/ $\alpha\text{-Fe}_2\text{O}_3$  and CuO-CeO<sub>2</sub> catalysts for the selective oxidation of carbon monoxide in excess hydrogen. *Catal. Today* **2002**, *75*, 157–167. [[CrossRef](#)]
- Sudarsanam, P.; Hillary, B.; Mallesham, B.; Rao, B.G.; Amin, M.H.; Nafady, A.; Alsalmé, A.M.; Reddy, B.M.; Bhargava, S.K. Designing  $\text{CuO}_x$  nanoparticle-decorated  $\text{CeO}_2$  nanocubes for catalytic soot oxidation: Role of the nanointerface in the catalytic performance of heterostructured nanomaterials. *Langmuir* **2016**, *32*, 2208–2215. [[CrossRef](#)]
- Mukherjee, D.; Rao, B.G.; Reddy, B.M. CO and soot oxidation activity of doped ceria: Influence of dopants. *Appl. Catal. B* **2016**, *197*, 105–115. [[CrossRef](#)]
- Davó-Quifonero, A.; Navlani-García, M.; Lozano-Castelló, D.; Bueno-López, A.; Anderson, J.A. Role of hydroxyl groups in the preferential oxidation of CO over copper oxide–cerium oxide catalysts. *ACS Catal.* **2016**, *6*, 1723–1731. [[CrossRef](#)]
- Di Benedetto, A.; Landi, G.; Lisi, L. Improved CO-PROX performance of CuO/CeO<sub>2</sub> catalysts by using nanometric ceria as support. *Catalysts* **2018**, *8*, 209. [[CrossRef](#)]
- Aneggi, E.; Boaro, M.; Leitenburg, C.D.; Dolcetti, G.; Trovarelli, A. Insights into the redox properties of ceria-based oxides and their implications in catalysis. *J. Alloys Compd.* **2006**, *408–412*, 1096–1102. [[CrossRef](#)]
- Bae, C.M.; Ko, J.B.; Kim, D.H. Selective catalytic oxidation of carbon monoxide with carbon dioxide, water vapor and excess hydrogen on CuO-CeO<sub>2</sub> mixed oxide catalysts. *Catal. Commun.* **2005**, *6*, 507–511. [[CrossRef](#)]
- Wang, J.; Pu, H.; Wan, G.; Chen, K.; Lu, J.; Lei, Y.; Zhong, L.; He, S.; Han, C.; Luo, Y. Promoted the reduction of  $\text{Cu}^{2+}$  to enhance CuO-CeO<sub>2</sub> catalysts for CO preferential oxidation in  $\text{H}_2$ -rich streams: Effects of preparation methods and copper precursors. *Int. J. Hydrogen Energy* **2017**, *42*, 21955–21968. [[CrossRef](#)]
- Shang, H.; Zhang, X.; Xu, J.; Han, Y. Effects of preparation methods on the activity of CuO/CeO<sub>2</sub> Catalysts for CO oxidation. *Front. Chem. Sci. Eng.* **2017**, *11*, 603–612. [[CrossRef](#)]

14. Cecilia, J.; Arango-Díaz, A.; Marrero-Jerez, J.; Núñez, P.; Moretti, E.; Storaro, L.; Rodríguez-Castellón, E. Catalytic behaviour of CuO-CeO<sub>2</sub> systems prepared by different synthetic methodologies in the CO-PROX reaction under CO<sub>2</sub>-H<sub>2</sub>O feed stream. *Catalysts* **2017**, *7*, 160. [[CrossRef](#)]
15. Liu, G.; Li, J.; Yang, K.; Tang, W.; Liu, H.; Yang, J.; Yue, R.; Chen, Y. Effects of cerium incorporation on the catalytic oxidation of benzene over flame-made perovskite La<sub>1-x</sub>Ce<sub>x</sub>MnO<sub>3</sub> catalysts. *Particuology* **2015**, *19*, 60–68. [[CrossRef](#)]
16. Liu, G.; Yue, R.; Jia, Y.; Ni, Y.; Yang, J.; Liu, H.; Wang, Z.; Wu, X.; Chen, Y. Catalytic oxidation of benzene over Ce-Mn oxides synthesized by flame spray pyrolysis. *Particuology* **2013**, *11*, 454–459. [[CrossRef](#)]
17. Zhao, F.; Li, S.; Wu, X.; Yue, R.; Li, W.; Chen, Y. Synergetic effect over flame-made manganese doped CuO-CeO<sub>2</sub> Nanocatalyst for enhanced CO oxidation performance. *RSC Adv.* **2019**, *9*, 2343–2352. [[CrossRef](#)]
18. Wang, Z.; Qu, Z.; Quan, X.; Li, Z.; Wang, H.; Fan, R. Selective catalytic oxidation of ammonia to nitrogen over CuO-CeO<sub>2</sub> mixed oxides prepared by surfactant-templated method. *Appl. Catal. B* **2013**, *134–135*, 153–166. [[CrossRef](#)]
19. Solsona, B.; Sanchis, R.; Dejoz, A.; García, T.; Ruiz-Rodríguez, L.; López Nieto, J.; Cecilia, J.; Rodríguez-Castellón, E. Total oxidation of propane using CeO<sub>2</sub> and CuO-CeO<sub>2</sub> catalysts prepared using templates of different nature. *Catalysts* **2017**, *7*, 96. [[CrossRef](#)]
20. Strobel, R.; Pratsinis, S.E. Flame aerosol synthesis of smart nanostructured materials. *J. Mater. Chem.* **2007**, *17*, 4743–4756. [[CrossRef](#)]
21. Feng, X.; Sayle, D.C.; Wang, Z.L.; Paras, M.S.; Santora, B.; Sutorik, A.C.; Sayle, T.X.T.; Yang, Y.; Ding, Y.; Wang, X.; et al. Converting ceria polyhedral nanoparticles into single-crystal nanospheres. *Science* **2006**, *312*, 1504. [[CrossRef](#)]
22. Liu, T.; Yao, Y.; Wei, L.; Shi, Z.; Han, L.; Yuan, H.; Li, B.; Dong, L.; Wang, F.; Sun, C. Preparation and evaluation of copper-manganese oxide as a high-efficiency catalyst for CO oxidation and NO reduction by CO. *J. Phys. Chem. C* **2017**, *121*, 12757–12770. [[CrossRef](#)]
23. Balducci, G.; Kaspar, J.; Fornasiero, P.; Graziani, M.; Islam, M.S. Surface and reduction energetics of the CeO<sub>2</sub>-ZrO<sub>2</sub> catalysts. *J. Phys. Chem. C* **1998**, *102*, 557–561. [[CrossRef](#)]
24. Fornasiero, P.; Balducci, G.; Di Monte, R.; Kašpar, J.; Sergio, V.; Gubitosa, G.; Ferrero, A.; Graziani, M. Modification of the redox behaviour of CeO<sub>2</sub> induced by structural doping with ZrO<sub>2</sub>. *J. Catal.* **1996**, *164*, 173–183. [[CrossRef](#)]
25. Dosa, M.; Piumetti, M.; Bensaid, S.; Andana, T.; Novara, C.; Giorgis, F.; Fino, D.; Russo, N. Novel Mn-Cu-containing CeO<sub>2</sub> nanopolyhedra for the oxidation of CO and diesel soot: Effect of dopants on the nanostructure and catalytic activity. *Catal. Lett.* **2017**, *148*, 298–311. [[CrossRef](#)]
26. Du, L.; Wang, W.; Yan, H.; Wang, X.; Jin, Z.; Song, Q.; Si, R.; Jia, C. Copper-ceria sheets catalysts: Effect of copper species on catalytic activity in CO oxidation reaction. *J. Rare Earths* **2017**, *35*, 1186–1196. [[CrossRef](#)]
27. Piumetti, M.; Bensaid, S.; Fino, D.; Russo, N. Nanostructured ceria-zirconia catalysts for CO oxidation: Study on surface properties and reactivity. *Appl. Catal. B* **2016**, *197*, 35–46. [[CrossRef](#)]
28. Binet, C.; Badri, A.; Boutonnet-Kizling, M.; Lavalley, J.C. FTIR study of carbon monoxide adsorption on ceria: CO carbonite dianion adsorbed species. *J. Chem. Soc. Faraday Trans.* **1994**, *90*, 1023–1028. [[CrossRef](#)]
29. Avgouropoulos, G.; Ioannides, T. Selective CO oxidation over CuO-CeO<sub>2</sub> catalysts prepared via the urea-nitrate combustion method. *Appl. Catal. A* **2003**, *244*, 155–167. [[CrossRef](#)]
30. Hočevar, S.; Krašovec, U.O.; Orel, B.; Aricó, A.S.; Kim, H. CWO of phenol on two differently prepared CuO-CeO<sub>2</sub> Catalysts. *Appl. Catal. B* **2000**, *28*, 113–125. [[CrossRef](#)]
31. Liu, W.; Flytzani-stephanopoulos, M. Total oxidation of carbon-monoxide and methane over transition metal fluorite oxide composite catalysts: II. catalyst characterization and reaction-kinetics. *J. Catal.* **1995**, *153*, 317–332. [[CrossRef](#)]
32. Xie, Y.; Yin, Y.; Zeng, S.; Gao, M.; Su, H. Coexistence of Cu<sup>+</sup> and Cu<sup>2+</sup> in star-shaped CeO<sub>2</sub>/Cu<sub>x</sub>O catalyst for preferential CO oxidation. *Catal. Commun.* **2017**, *99*, 110–114. [[CrossRef](#)]
33. Gómez, L.E.; Miró, E.E.; Boix, A.V. Spectroscopic characterization of Mn-Co-Ce mixed oxides, active catalysts for COPROX reaction. *Int. J. Hydrogen Energy* **2013**, *38*, 5645–5654. [[CrossRef](#)]
34. Qi, L.; Yu, Q.; Dai, Y.; Tang, C.; Liu, L.; Zhang, H.; Gao, F.; Dong, L.; Chen, Y. Influence of cerium precursors on the structure and reducibility of mesoporous CuO-CeO<sub>2</sub> catalysts for CO oxidation. *Appl. Catal. B* **2012**, *119–120*, 308–320. [[CrossRef](#)]

35. Li, S.; Wang, H.; Li, W.; Wu, X.; Tang, W.; Chen, Y. Effect of Cu substitution on promoted benzene oxidation over porous CuCo-based catalysts derived from layered double hydroxide with resistance of water vapor. *Appl. Catal. B* **2015**, *166–167*, 260–269. [[CrossRef](#)]
36. Zhang, R.; Teoh, W.Y.; Amal, R.; Chen, B.; Kaliaguine, S. Catalytic reduction of NO by CO over Cu/Ce<sub>x</sub>Zr<sub>1-x</sub>O<sub>2</sub> prepared by flame synthesis. *J. Catal.* **2010**, *272*, 210–219. [[CrossRef](#)]
37. Dow, W.P.; Huang, T.J. Effects of oxygen vacancy of yttria-stabilized zirconia support on carbon monoxide oxidation over copper catalyst. *J. Catal.* **1994**, *147*, 322–332. [[CrossRef](#)]
38. Piumetti, M.; Bensaid, S.; Russo, N.; Fino, D. Nanostructured ceria-based catalysts for soot combustion: Investigations on the surface sensitivity. *Appl. Catal. B* **2015**, *165*, 742–751. [[CrossRef](#)]
39. Zhu, P.; Li, J.; Zuo, S.; Zhou, R. Preferential oxidation properties of CO in excess hydrogen over CuO-CeO<sub>2</sub> catalyst prepared by hydrothermal Method. *Appl. Surf. Sci.* **2008**, *255*, 2903–2909. [[CrossRef](#)]
40. Delimaris, D.; Ioannides, T. VOC oxidation over CuO-CeO<sub>2</sub> catalysts prepared by a combustion Method. *Appl. Catal. B* **2009**, *89*, 295–302. [[CrossRef](#)]
41. Jia, A.P.; Deng, Y.; Hu, G.S.; Luo, M.F.; Lu, J.Q. Kinetic and activity study of CO oxidation over CuO-MnO<sub>x</sub>-CeO<sub>2</sub> catalysts. *React. Kinet. Mech. Catal.* **2015**, *117*, 503–520. [[CrossRef](#)]
42. Piumetti, M.; Bensaid, S.; Andana, T.; Russo, N.; Pirone, R.; Fino, D. Cerium-copper oxides prepared by solution combustion synthesis for total oxidation reactions: from powder catalysts to structured reactors. *Appl. Catal. B* **2017**, *205*, 455–468. [[CrossRef](#)]
43. Sun, S.; Mao, D.; Yu, J.; Yang, Z.; Lu, G.; Ma, Z. Low-temperature CO oxidation on CuO/CeO<sub>2</sub> catalysts: The significant effect of copper precursor and calcination temperature. *Catal. Sci. Technol.* **2015**, *5*, 3166–3181. [[CrossRef](#)]
44. Chen, G.; Xu, Q.; Yang, Y.; Li, C.; Huang, T.; Sun, G.; Zhang, S.; Ma, D.; Li, X. Facile and mild strategy to construct mesoporous CeO<sub>2</sub>-CuO nanorods with enhanced catalytic activity toward CO oxidation. *ACS Appl. Mater. Interfaces* **2015**, *7*, 23538–23544. [[CrossRef](#)]
45. Xiao, W.; Yang, S.; Zhang, P.; Li, P.; Wu, P.; Li, M.; Chen, N.; Jie, K.; Huang, C.; Zhang, N.; et al. Facile synthesis of highly porous metal oxides by mechanochemical nanocasting. *Chem. Mater.* **2018**, *30*, 2924–2929. [[CrossRef](#)]
46. Spezzati, G.; Benavidez, A.D.; DeLaRiva, A.T.; Su, Y.; Hofmann, J.P.; Asahina, S.; Olivier, E.J.; Neethling, J.H.; Miller, J.T.; Datye, A.K.; Hensen, E.J.M. CO oxidation by Pd supported on CeO<sub>2</sub>(100) and CeO<sub>2</sub>(111) facets. *Appl. Catal. B Environ.* **2019**, *243*, 36–46. [[CrossRef](#)]
47. Wang, H.; Mao, D.; Qi, J.; Zhang, Q.; Ma, X.; Song, S.; Gu, L.; Yu, R.; Wang, D. Hollow multishelled structure of heterogeneous Co<sub>3</sub>O<sub>4</sub>-CeO<sub>2-x</sub> nanocomposite for CO catalytic oxidation. *Adv. Funct. Mater.* **2019**, 1806588. [[CrossRef](#)]
48. Gong, S.; Chen, J.; Wu, X.; Han, N.; Chen, Y. In-situ synthesis of Cu<sub>2</sub>O/reduced graphene oxide composite as effective catalyst for ozone decomposition. *Catal. Commun.* **2018**, *106*, 25–29. [[CrossRef](#)]
49. Sanchez, M.G.; Gazquez, J.L. Oxygen vacancy model in strong metal-support interaction. *J. Catal.* **1987**, *104*, 120–135. [[CrossRef](#)]
50. Wan, H.; Wang, Z.; Zhu, J.; Li, X.; Liu, B.; Gao, F.; Dong, L.; Chen, Y. Influence of CO pretreatment on the activities of CuO/γ-Al<sub>2</sub>O<sub>3</sub> catalysts in CO+O<sub>2</sub> reaction. *Appl. Catal. B* **2008**, *79*, 254–261. [[CrossRef](#)]
51. Zhang, Z.; Zhu, Yi.; Asakura, H.; Zhang, B.; Zhang, J.; Zhou, M.; Han, Y.; Tanaka, T.; Wang, A.; Zhang, T.; et al. Thermally stable single atom Pt/M-Al<sub>2</sub>O<sub>3</sub> for selective hydrogenation and CO oxidation. *Nat. Commun.* **2017**, *8*, 16100. [[CrossRef](#)] [[PubMed](#)]
52. Gamarra, D.; Martínez-Arias, A. Preferential oxidation of CO in rich H<sub>2</sub> over CuO/CeO<sub>2</sub>: Operando-drifts analysis of deactivating effect of CO<sub>2</sub> and H<sub>2</sub>O. *J. Catal.* **2009**, *263*, 189–195. [[CrossRef](#)]
53. Binet, C.; Daturi, M.; Lavalley, J.C. Ir study of polycrystalline ceria properties in oxidised and reduced states. *Catal. Today* **1999**, *50*, 207–225. [[CrossRef](#)]

